Linking volcano morphology and elastic thickness on Mars

DAVID KRASNER
GEOL394
DR. LAURENT MONTESI
FALL 2014

Abstract

A range of volcanic morphologies is observed across the surface of the planet Mars. These volcanoes exert large vertical loads atop the lithosphere, which responds be compensating and deflecting downward. The flexure-induced stresses strongly influence magma ascent through the plate, from the mantle to the surface. This broad range of volcanic edifice profiles is related to characteristics of the underlying lithosphere. In my GEOL394 project, I investigate a relationship between flexural stresses and how they control the shapes of volcanic edifices on Mars.

I hypothesize and investigate a relationship between the lithospheric elastic thickness and volcano morphology on Mars. For lithospheres with the largest values of T_e (i.e., $T_e > 40$ km), I predict that younger, conical volcanoes with high topographic relief and steeply graded flanks will form atop the plate. In this case, all magma ascent criteria will be satisfied over the entire lithosphere, permitting uninhibited flow to the surface to form these steep edifices. For the lowest values of T_e (i.e., $T_e < 15$ km), widely spaced zones of magma ascent are caused by short-wave deflections in the lithosphere, forming flat or annular volcanoes with low topographic relief and broad radii. For intermediate values of T_e (i.e., $15 < T_e < 40$ km), high stress gradients will cut off magma ascent beneath the summit of the growing edifice, resulting in domical shapes (McGovern, et al., 2013).

These volcanoes can be used as a tool to help us understand the planets current condition, its history since formation, and how it compares to Earth. Terrestrial volcanoes are a key component of a planet's dynamical system, being mechanisms of heat transfer, volatile transport, atmosphere production, and magma/mass emplacement atop the lithosphere. This last aspect will provide insight to Mars' thermal history and evolution over time. A lithosphere thickens as time progresses, and the rate of thickening correlates with the rate of cooling over time.

When an overlying load is placed atop a plate of uniform material and thickness, the plate bends to compensate and experiences a flexural response with a coinciding a flexure-induced stress field local to the loading. This stress tensor influences local tension and compression in the plate, which directly affects the formation of dikes in the area of loading. Furthermore, the orientations of these dikes dictate where subsequent eruptions and magma emplacements will occur. The elastic thickness and flexural rigidity change the orientation of the stresses within the plate, which change the formation and orientation of dikes surrounding the load.

The flexure from various volcanic profiles has been observed on Venus (McGovern, et al., 2013), with the flexure-induced stress field, and magma ascent modeled and observed. I generate a self-consistent model by placing incremental loads atop a thin elastic plate of a given thickness. Subsequent magma ascent is guided by flexure-induced stresses. My models show a correlation between the morphology and evolution of the growing volcanic edifice for given elastic thicknesses. These profiles are then compared to the variety of volcanoes that are seen across the Martian landscape. Future implications for a volcanic and thermal history of the planet are drawn from this experiment.

1. Table of Contents

2. Introduction

2.1 Morphological Classification of volcanoes

The terrestrial planets of our solar system feature various forms of volcanic edifices and related surficial structures. There are volcanoes of various shapes and sizes on Mars that are of interest to me in this project. The Tharsis bulge is a large volcanic province that is centered near the equator in the planets western hemisphere. The largest volcanoes in the solar system are located on Tharsis: the shield volcanoes known as the Tharsis Mons: Pavonis Mons, Ascraeus Mons, and Arsia Mons *(Figure 1)* and also the largest volcano on the planet, Olympus Mons. Olympus Mons is almost 100 times larger than the largest shield volcano on Earth, Mauna Loa. Mars is thought to lack plate tectonics; therefore the dominant form of volcanism is hotspot volcanism. Without known plate boundaries through which the magma can reach the surface, long-lived mantle upwellings cause the formation of these broad shield volcanoes. These hotspots paired with the low gravitational acceleration on the surface (3.711 $\frac{m}{s^2}$) permit these volcanoes to reach immense heights. According to Werner (2009), the shield edifices of the Tharsis Montes were formed ~3.55 Ga, and have been episodically active until ~100 Ma.

The low-lying Patera-volcanoes, such as Tyrrhena Patera *(Figure 2)* located in the heavily cratered, topographic high, southern hemisphere of the planet, are characterized by their low topographic profile, broad radial extent, and ancient ages. Werner (2009) estimates the time of emplacement of Tyrrhena Patera to have been before 3.9 Ga. Tyrrhena Patera has radial extent of ~600 km and a small topographic relief of ~1.5 km (Werner, 2009). The flank of the Patera is heavily eroded with channels that radiate from the summit region. The volcano is likely to be composed of pyroclastic deposits that have been easily eroded. The eruption style of this Patera volcano is much different from the fluid lavas that likely built up the shield volcanoes of Tharsis.

The Elysium volcanic province *(Figure 3)* is the second largest volcanic structure after Tharsis. It is located in the eastern hemisphere atop the northern

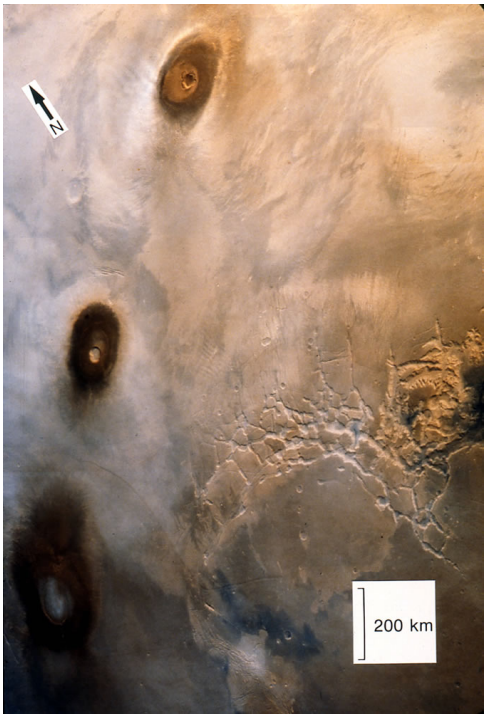

Figure 1: The Tharsis Montes (L-R) Arsia Mons, Pavonis Mons, Ascraeus Mons are shield volcanoes on the Tharsis bulge. All have an elevation of ~15km and a radial extent ranging from 350-450km.
http://lpi.usra.edu

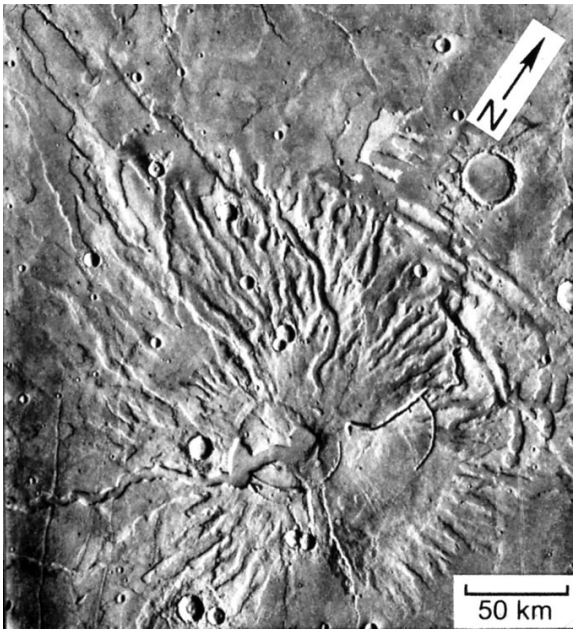

Figure 2: Tyrrhena Patera lies in the southern highlands of Mars. Being emplaced before 3.9 Ga, this volcano provides insight to early forms of Martian volcanism. Its low topographic profile, and heavily eroded channels are signs of a pyroclastic style deposition/eruption. Paterae volcanoes can be classified as flat in profile.
http://lpi.usra.edu

lowlands. The volcanoes of the province include (from N to S) Hecates Tholus, Elysium Mons, and Albor Tholus. Elysium Mons has a steeper slope (~10º) than the volcanoes of Tharsis, a elevation of ~14 km, was emplaced ~3.5 Ga with the most recent resurfacing event ~1.6 Ga (Werner, 2009). The two Tholi volcanoes have smaller relief ~5.5 km, and radial extent of ~150 km. They have convex slopes with ~5º angles. Summit activity in the caldera of Albor Tholus is thought to have been active until 500 Ma (Werner, 2009)

Volcanic profiles can be characterized in terms of edifice radius, height, slope, and shape, leading to

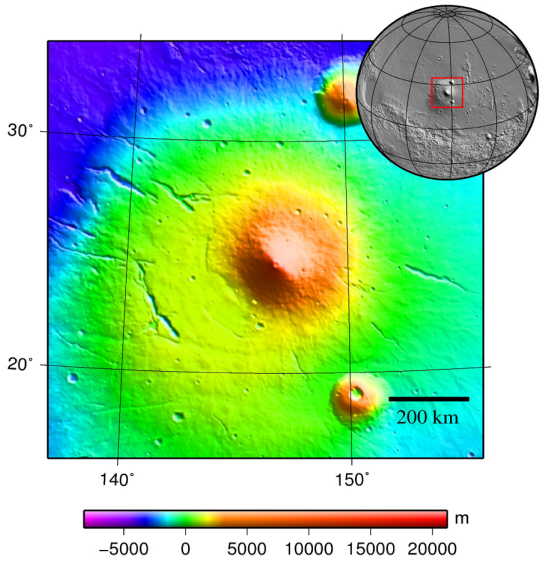

Figure 3: The Elysium volcanic province lies in the planets eastern hemisphere in the northern lowlands. It hosts the volcanoes (from N to S) Hecates Tholus, Elysium Mons, and Albor Tholus. These volcanoes be classified as conical n profile.

http://lpi.usra.edu

three general categories of volcano morphology. Conical edifices have a point-like apex and a steeply sloped profile. The volcanoes on Elysium can be classified as cone volcanoes, they have high topographic relief, and steep sloping sides *(Figure 3)*. Domical volcanoes have a much more gradual slope, and a generally flat, tabletop character at higher elevations. Olympus Mons can be considered a dome volcano *(Figure 4)*. Flat volcanoes have a very diffuse topographic profile, a large breadth of radial extent, and are at times ring-like in shape; those of which are known as annular in profile. Paterae volcanoes on Mars can be classified as flat profiles because of their broad radial extent, and low topographic relief *(Figure 2)*.

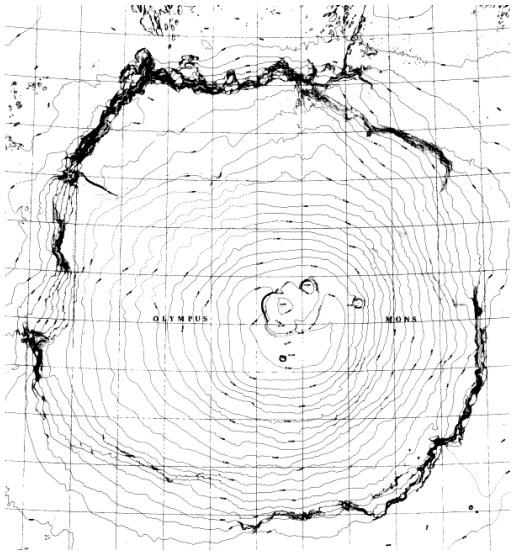

Figure 4: Olympus Mons is characterized by its large radial extent, its high elevation, and its gradually sloping flanks. This can be considered a domical edifice.

Sherman, et al., (1981)

2.2 Deformation and volcano growth

When an overlying load (i.e. a mountain, glacier, or volcano) is emplaced atop the surface of a terrestrial body, the underlying lithosphere experiences flexure and must deform to compensate for the mass of the overlying topographic load (Watts, 2001). Over geologic time scales, the lithosphere is known to deform elastically and can bend under an overlying load. When deformation is relatively small, the lithosphere can be considered a thin elastic shell experiencing deflection in vertical z-axis direction (Comer, 1983). The overlying load pushes the lithosphere downward, and a resultant stress field is generated within the plate. In the case of a volcanic load, these stress fields constrain both how and where magma ascent occurs. Magma ascent criteria dictates where rising magma will be emplaced. The emplacement of magma influences the shape, slope, and other physical features of the growing volcano, modifying the evolving flexural deflection of the plate.

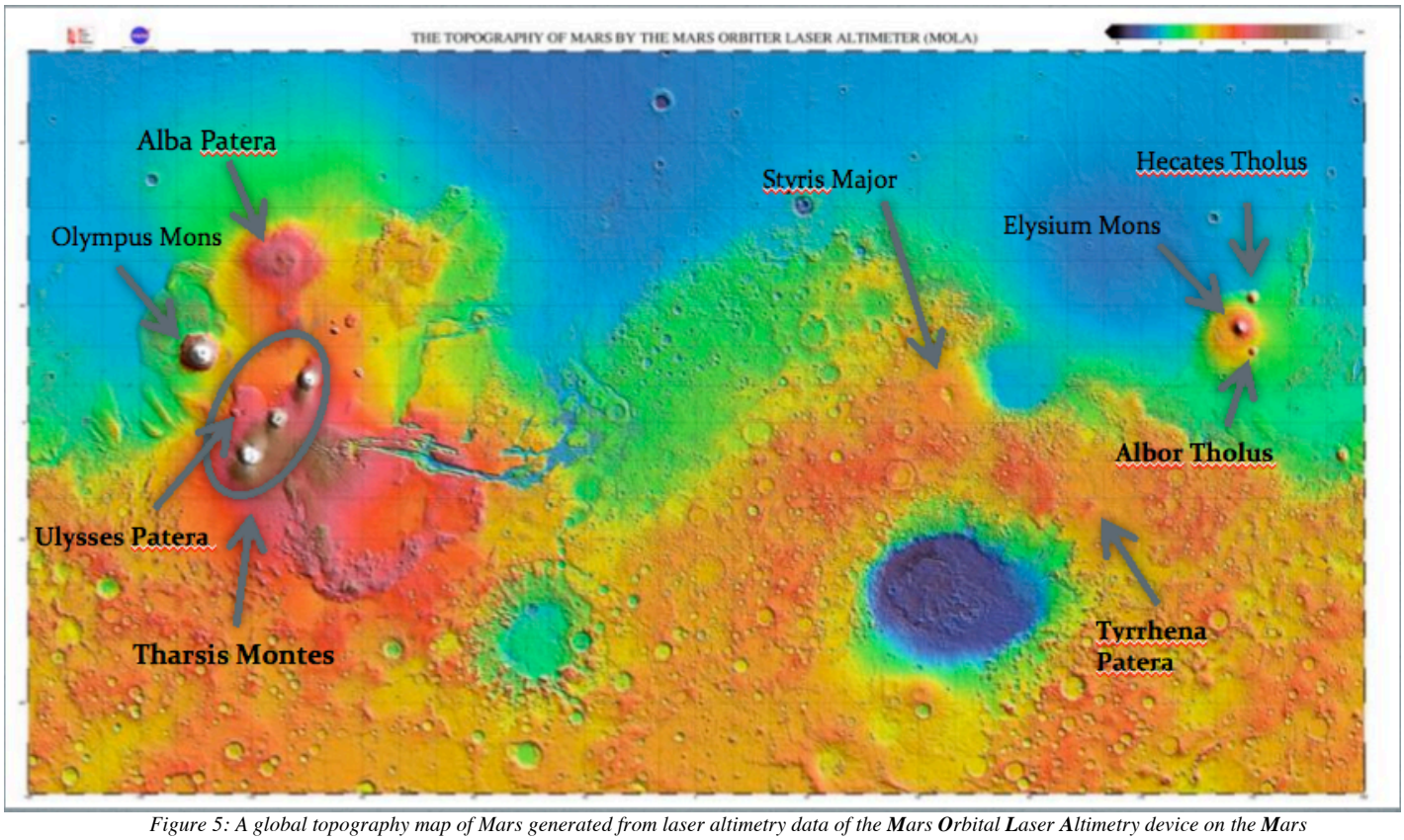

*Figure 5: A global topography map of Mars generated from laser altimetry data of the **M**ars **O**rbital **L**aser **A**ltimetry device on the **M**ars **G**lobal **S**urveyor. Noted are volcanoes that will be of focus*

McGovern et al. (2013) show that, on Venus, volcanoes of different shapes produce different patterns of magma ascent that may or may not preserve the shape of the edifice. They found that conical volcanoes are consistent with a thick plate, but that flat or ring edifices are consistent with thin elastic plates. Domical volcanoes are intermediate between the other two. However, they only consider a fully formed edifice. I instead model the growth of the edifice in several increments to test what kind of volcano is possible for various elastic plate thicknesses and apply these models to Mars.

In my senior thesis project I am studying the stress field induced by volcanic loads placed atop a thin elastic shell. These stresses fields constrain the ascent of underlying magma (Rubin 1995), and where, in the crust, the emplacement of magma occurs. The emplacement of the magma is considered to be atop the surface of the plate. As each volcanic load is emplaced incrementally, a growing volcanic profile is observed. Based on the work of McGovern et al. (2013), I hypothesize that conical volcanoes will be produced on thick elastic plates and flat volcanoes on thin plates. Thus it will be possible to constrain the elastic thickness of various location on Mars based on the shape of volcanoes that are observed there.

2.3 Implications

Volcanism on Mars was widespread from the planets formation at 4.5 Ga, until ~3.0 Ga, since then, the planet has been significantly less active, with noted late-Amazonian pyroclastic deposits, and lava flows within the Arsia Mons caldera that are no more than 100-200 million years old (Hartmann, et al., 1999). The volcanic diversity is influenced by different lithospheric characteristics such as the flexural rigidity and elastic thickness of the lithosphere, and the rate of thickening of the lithosphere. Rates of cooling and thickening of the lithosphere can be implied from a volcanic and thermal history of Mars. Comer et al., (1985) observe concentric grabben surrounding the topographic loads of volcanoes. They correlated the

spacing of these grabben to the age of emplacement. McGovern et al. (2002) estimated the elastic thickness and deflection necessary to support a load by measuring the planets topographic distribution on regional and global scales. By comparing different regions and edifices formed at different epochs, it will be possible to better constrain the thermal evolution of the planet and spatial variations of lithosphere structure. Furthermore, new constraints on the elastic thickness of Mars can provide a more detailed history of the thickening and cooling lithosphere.

3. Experiment Design

The volcanic growth model is written and generated in MATLAB. In a self-consistent approach, incremental loads are emplaced atop a model of a terrestrial lithosphere, modeled as a thin elastic shell, with the flexure-induced stress guiding magma ascent and the subsequent emplacement of each additional load.

The maximum deflection of an elastic plate is described by Watts (2001):

Equation 1: $$w_{max} = \frac{P}{8\alpha^2(\rho_{mantle}-\rho_{infill})g}$$

The flexure of a thin elastic shell is given by:

Equation 2: $$\nabla^4 w + \alpha^{-4} w = q/D$$

w_{max} is the maximum deflection, P is the weight (force) of a concentrated load, ∇^4 is a differential operator called a biharmonic operator, it is equivalent to the square of the Laplacian operator, the divergence of a gradient of a scalar function. w is the vertical deflection of the plate, α is the flexural parameter, D is the flexural rigidity, and q is the load itself (Brotchie and Silvester 1969).

D is defined as:

Equation 3: $$D = \frac{EH^3}{12(1-\nu^2)}$$

α is defined as:

Equation 4: $$\alpha = \left[\frac{D}{(\rho_{mantle}-\rho_{infill})g}\right]^{1/4}$$

where α is the three-dimensional flexural parameter, H is the thickness of the plate, E is Young's Modulus, ν is Poisson's ratio, $\rho_{mantle} - \rho_{infill}$ is the density difference of the materials above and below the plate, and g is acceleration due to gravity.

In (2), $D\nabla^4 w$ is the bending moment of the thin elastic plate, and $D\alpha^{-4}w$ is the hydrostatic restoring force of the plate resultant from density variations above and below the layer. The flexure equation admits well-known solutions, discussed in the next section, for simple load geometries such as a point load and a line load (Watts 2001).

3.1 Flexure

3.1.1 Line Load

In the presence of a line load that extends infinitely in the y-direction, a solution exists that is dependent on x, and is symmetric with respect to y. In this case, (2) can be simplified to:

Equation 5: $$\frac{\partial^4 w}{\partial x^4} + \alpha^{-4} w = \frac{q}{D}$$

Applying a fixed displacement $w=w_0$ at $x=0$ and $w=0$ at $x=\pm\infty$, (5) admits the following analytical solution:

Equation 6:
$$w = w_0 e^{-x\beta}[\cos(\beta x) + \sin(\beta x)]$$

Where α is the flexural wavelength that controls the length scale of the flexural response.

Equation 7: $$\beta = \frac{\sqrt{2}}{\alpha}$$

The downward deflection at x=0 is flanked by uplift at a distance bulge at x=± $\pi\alpha$. The amplitude of the deflection decreases exponentially and is essentially negligible for $|x| \geq 2\pi\alpha$.

The maximum flexure (y_{max}) of an infinite beam from a concentrated load P is similar to (6):

Equation 8:
$$y_{max} \frac{P\vartheta}{2(\rho_{mantle}-\rho_{infill})g} e^{-\vartheta x}[\cos(\vartheta x) + \sin(\vartheta x)]$$

ϑ is defined as:

Equation 9: $$\vartheta = \frac{1}{\alpha}$$

3.1.2 Point Load

In the presence of a point load at any point in the (x,y) plane, the solution is axisymmetric about the z-axis. The solution for (2) in this case will be:

Equation 10: $$w = w_k \mathrm{kei}\left(\frac{r}{\alpha}\right)$$

With w_k defined as $w_k = w_0/\mathrm{kei}(0)$. Note that the equation only depends on r, the radial distance from the point of displacement. Kei is the imaginary part of the modified Bessel function of the second kind. A Bessel function is a mathematical tool used to obtain separable solutions to Laplace's equations, being useful in wave propagation equations. We have defined kei as function in MATLAB, with values obtain from Weller (2012) (Appendix A).

3.1.3 Flexural Models

MATLAB scripts are used to generate models for infinite line loads, and point loads for three randomly selected points. The solution for a line load in 2-D *(5)*, with three randomly selected loads is depicted in *Figure 6*. A 3-D visualization, with the lines extending infinitely in the y-direction, is depicted in *Figure 7*.

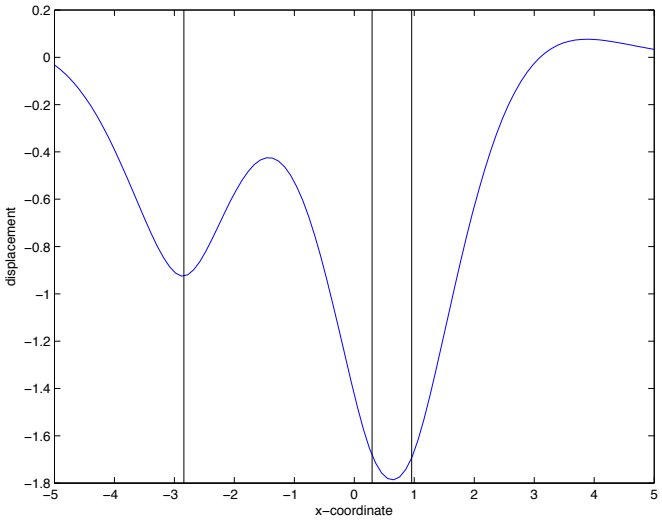

(Figure 6: Three line loads emplaced on a 1-D plate

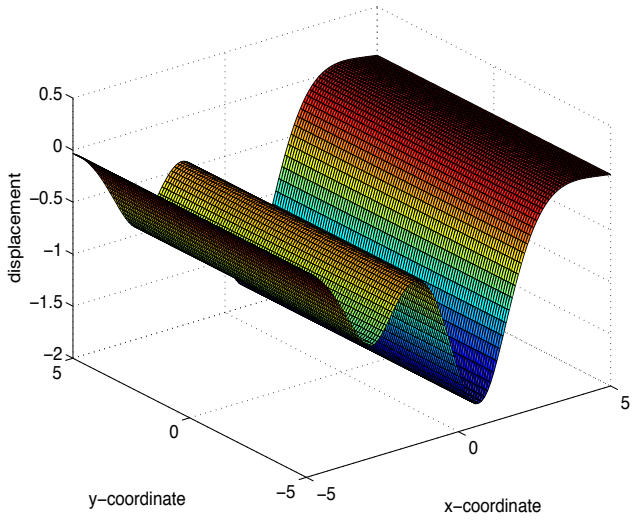

(Figure 7: Three line loads emplaced on a 2-D plate, extending infinitely in the y-direction)

The solution for a point load (6), with a top-down view of three randomly selected points, is depicted in *Figure 8*. The contour lines represent the displacement in the z-direction of each of these points. A 3-D visualization of this one point is shown in *Figure 9*.

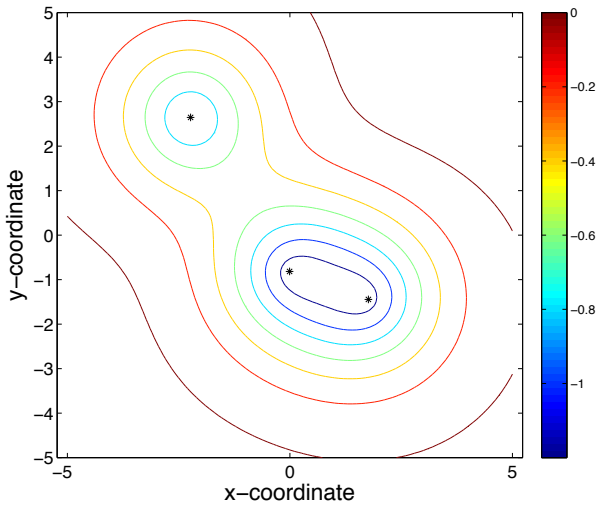

Figure 8: Contour map visualization of three randomly selected point loads. Contour lines represent contour of displacement in z-direction into the page)

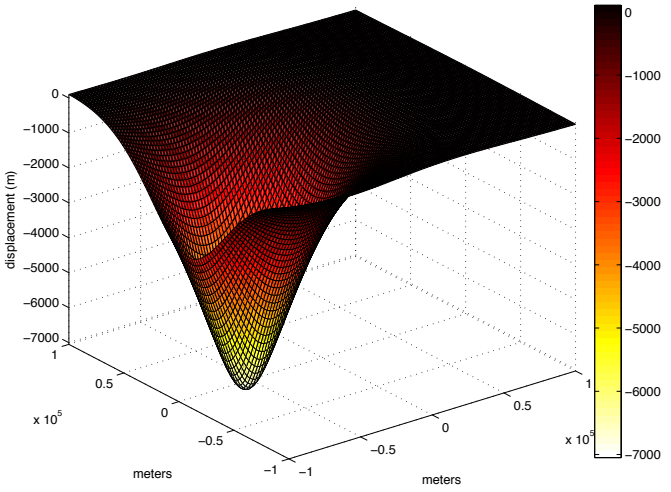

Figure 9: A 3-D visualization of one point of displacement

The mesh of the surfaces shown in *Figures 7-9* is composed of a domain in which the data points of the flexural events are contained. When we prompt the script to initially include more points in the grid, the resolution of the surface becomes finer. As the grid increases in resolution, the more precise the visualization of the solution becomes

3.1.4 Flexural Forebulge

The flexural forebulge can be found directly adjacent to, in front of, an area lithospheric loading. This forebulge is a slight uplift caused by the flexural rigidity of the plate itself, and furthermore, the density contrasts between the plate and the medium that surrounds it. In our case of lithospheric loading, the density contrast lies between the density of the plate, the density of the infilling material, and the density of the air/medium above the plate.

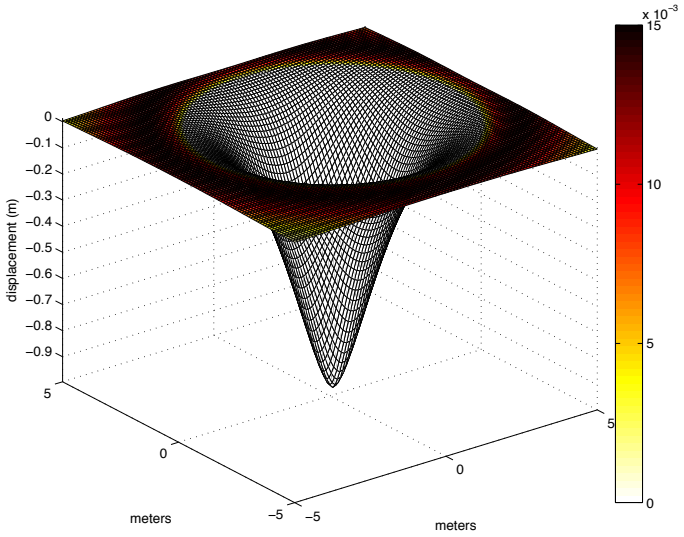

Figure 10: 3-D visualization of one point of displacement a seen in Figure 5, with limits put on the scale of the colormap to accentuate the flexural forebulge. Note that the scale of magnitude of the forebulge is very small (10^{-4} m) compared to that of the overall displacement from the load. As the thickness of the plate changes, the flexural rigidity of the plate with increase, therefore increasing the magnitude of the forebulge.

Due to the waveform nature of our flexural/displacement equation, the distance from the load to the maximum amplitude of the forebulge can be determined where the slope of the flexural response is zero. The point at which the slope is zero, and where the forebulge height is at its maximum, is found at a flexural half-wavelength ($\frac{\alpha}{2}$), or at a distance of $x = \pi a$ from the load. The amplitude of the forebulge is significantly smaller than that of the depression in the lithosphere in the presence of a point load. As well as being characterized as having a small amplitude, the magnitude of the forebulge decays exponentially with increasing distance from the area of loading, with the forebulge negligible at distances greater than $|x| \geq 2\pi a$.

3.2 Stress Fields

3.2.1 Flexure Induced Stress

Stress is expressed as a nine-component symmetric tensor:

Equation 11:

$$\boldsymbol{\sigma} = \begin{bmatrix} \sigma_{xx} & \sigma_{xy} & \sigma_{xz} \\ \sigma_{xy} & \sigma_{yy} & \sigma_{yz} \\ \sigma_{xz} & \sigma_{yz} & \sigma_{zz} \end{bmatrix}$$

In linear elasticity, μ and λ are the Lamé parameters that parameterize the elastic moduli of homogenous isotropic solids. They are related to the Young's modulus E and Poisson ratio υ of a medium by:

Equation 12: $$\lambda = \frac{E\nu}{(1+\nu)(1-2\nu)}$$

Equation 13: $$\mu = \frac{E}{2(1+\nu)}$$

Flexure is defined by the spatially variable vertical displacement field, $w(x,y)$, which is very small compared to radius of the Earth. Therefore, parallel straight lines, or fibers, in the undeformed plate remain approximately straight and parallel even when flexed. Moreover, slopes are also assumed to be very small. Therefore, the shear stresses σ_{xz} and σ_{yz} are negligible.

The bending of the plate generates horizontal stresses that shorten and lengthen fibers on the concave and convex sides of the bent plate. Stress increases in magnitude with z_f, the distance from the neutral fiber (also the mid-point of the plate) and change sign on either side of the neutral fiber. The components of Equation 11 being defined as:

Equation 14:

$$\sigma_{xx} = z_f \left[(\lambda + 2\mu) \frac{^2w}{\partial x^2} + \lambda \frac{\partial^2 w}{\partial y^2} \right]$$

Equation 15:

$$\sigma_{yy} = z_f \left[\lambda \frac{\partial^2 w}{\partial x^2} + (\lambda + 2\mu) \frac{\partial^2 w}{\partial y^2} \right]$$

Equation 16:

$$\sigma_{xy} = \sigma_{yx} = 2\mu z_f \frac{\partial^2 w}{\partial x \partial y}$$

The vertical stress σ_{zz} is the combination of the lithostatic pressure and a flexure-related stress generated by Poisson effect in response to the horizontal normal stresses.

Equation 17:

$$\sigma_{zz} = \rho_v g h_v + \rho_l g \left(\frac{H}{2} - z_f \right) + z_f \lambda \left(\frac{\partial^2 w}{\partial x^2} + \frac{\partial^2 w}{\partial y^2} \right)$$

Here, h_v is the height of the volcanic load; ρ_v and ρ_l are the densities of the volcanic load and the lithosphere, respectively. If deformation is small, the lithostatic stress dominates (17).

3.2.2 Numerical Implementation

Analytical or semi-analytical solutions for the stress field associated with plate bending in the simple cases of a line load or a point load are available in the literature (e.g., Comer, 1983). However, we need to evaluate stress in a more general case of an arbitrary load. To do this, we use a finite difference approximation to the stress equations above.

The displacement field $w(x,y)$ is defined over a set of sampling points that form a regular Cartesian grid, with spacing h between any given two points. Each point is associated the indices i and j in the x and y direction, respectively. The first and second derivatives of w are evaluated using the nine points that surround an evaluation point (x_i, y_j). The slope is given by

Equation 18:

$$\left. \frac{\partial w}{\partial x} \right|_{i,j} = \frac{w_{i+1,j} - w_{i-1,j}}{2h}$$

Equation 19:

$$\left. \frac{\partial w}{\partial y} \right|_{i,j} = \frac{w_{i,j+1} - w_{i,j-1}}{2h}$$

Equation 20:

$$\left.\frac{\partial^2 w}{\partial x^2}\right|_{i,j} = \frac{\left.\frac{\partial w}{\partial x}\right|_{i+\frac{1}{2},j} - \left.\frac{\partial w}{\partial x}\right|_{i-\frac{1}{2},j}}{h} = \frac{w_{i+1,j} - 2w_{i,j} + w_{i-1,j}}{h^2}$$

Equation 21:

$$\left.\frac{\partial^2 w}{\partial y^2}\right|_{i,j} = \frac{\left.\frac{\partial w}{\partial y}\right|_{i,j+\frac{1}{2}} - \left.\frac{\partial w}{\partial y}\right|_{i,j-\frac{1}{2}}}{h} = \frac{w_{i,j+1} - 2w_{i,j} + w_{i,j-1}}{h^2}$$

Equation 22:

$$\left.\frac{\partial^2 w}{\partial x \partial y}\right|_{i,j} = \frac{\left.\frac{\partial w}{\partial x}\right|_{i,j+1} - \left.\frac{\partial w}{\partial x}\right|_{i,j-1}}{2h} = \frac{w_{i+1,j+1} - w_{i-1,j-1} - w_{i+1,j-1} + w_{i-1,j-1}}{4h^2}$$

The accuracy of the numerical scheme presented above is evaluated using predefined displacement fields for which there is an analytical solution for the first and second derivatives. I input a known *w* into (14)-(17) and compare the numerical and analytical solutions to measure the relative error.

Equation 23: $w = r = \sqrt{x^2 + y^2}$

Equation 24: $\frac{\partial^2 w}{\partial x^2} = \frac{x^2}{r^3}$

Equation 25: $\frac{\partial^2 w}{\partial y^2} = \frac{y^2}{r^3}$

Equation 26: $\frac{\partial^2 w}{\partial xy} = \frac{xy}{r^3}$

To measure the relative error of our analytical model, I implemented the above numerical solutions for a known *w* into the script and compare the solution with the analytical solution using (27).

Equation 27:

$$\text{Error} = \frac{Numerical - Analytical}{Analytical}$$

3.2.3 Examples of Surface Stress

The stress fields associated with the surface displacement generated by one randomly generated point load are shown in *Figures 6-11*. See *Table* 1 for input parameters.

Applying (16)-(17) to a MATLAB function, σ_{xy}, and σ_{zz} stress fields are visualized.

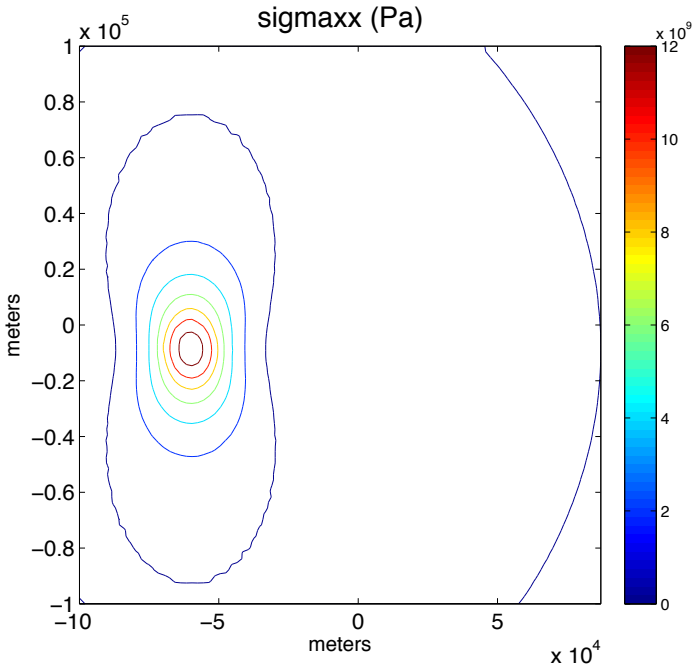

*Figure 10: Stress σ_{xx} at the surface of the plate associated with the displacement field generated by one randomly located point load (See Figure 5). Note tension n in the y range, and compression in the x range. Source **w** is found (7) and applied to equation (14).*

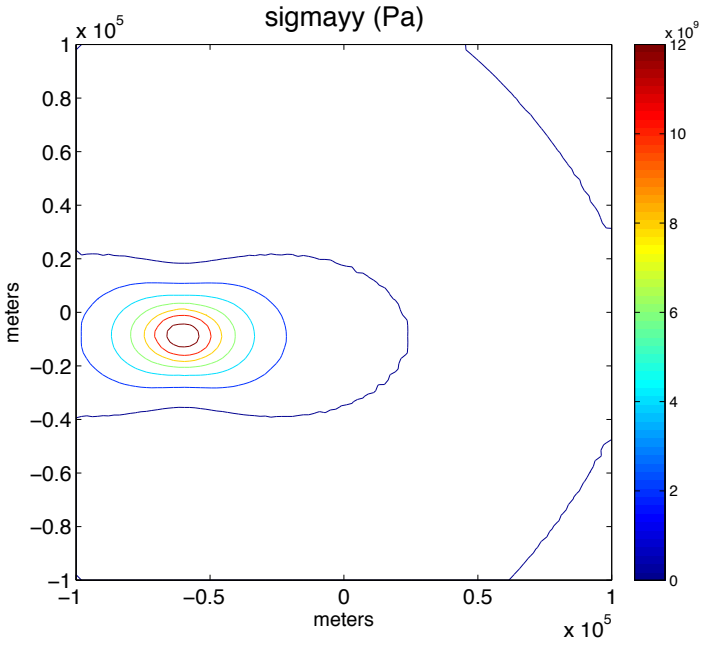

*Figure 11: Stress σ_{yy} at the surface of the plate associated with the displacement field generated by one randomly located point load (See Figure 5). Note tension in the y range, and extension in the x range. Source **w** is found in (7) and applied to (15)*

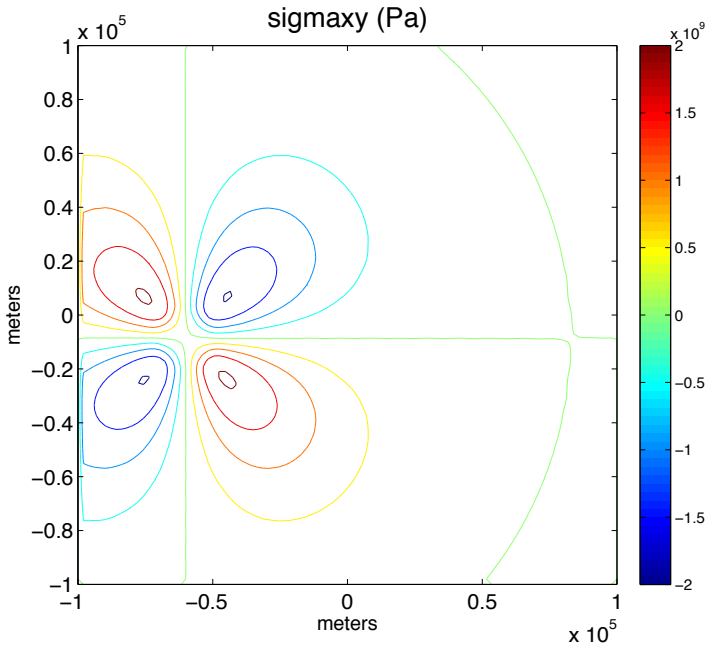

*Figure 12: Stress σ_{xy} at the surface of the plate associated with the displacement field generated by one randomly located point load (See Figure 5). Source **w** is found in (7) and applied to (16)*

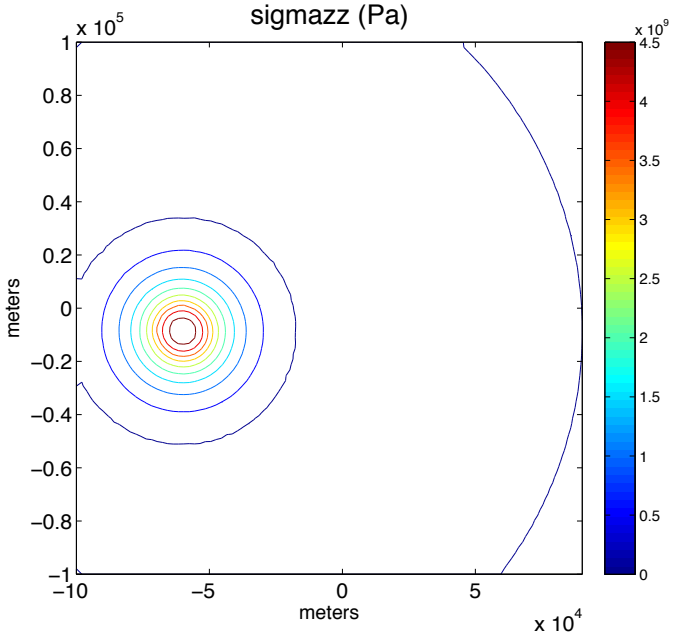

*Figure 13: Stress σ_{zz} at the surface of the plate associated with the displacement field generated by one randomly located point load (See Figure 5). Note uniform gradient in both the y range, and in the x range at radial distances from points of displacement. Source **w** is found in (7) and applied to (17))*

As expected, the errors calculated from (27) are practically zero throughout the planes in *Figures 14-17*. This shows that the error within the analytic model is extremely small.

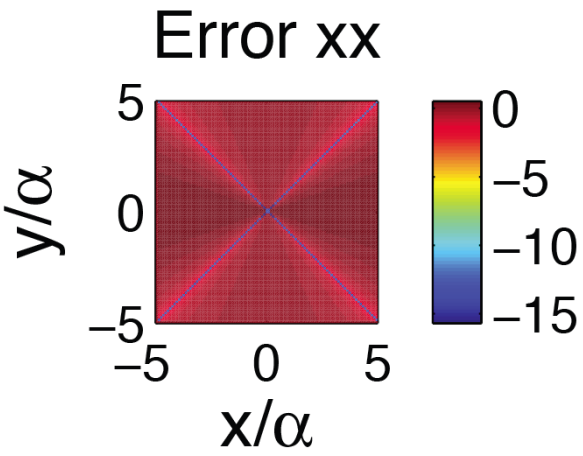

Figure 14: σ_{xx} error using Equation 27. Note that practically all points in the field are 0. The points that are not 0 resemble the small amount of error in our model. Visualization is plotted on a $\log_{10}$ scale to accentuate detail.

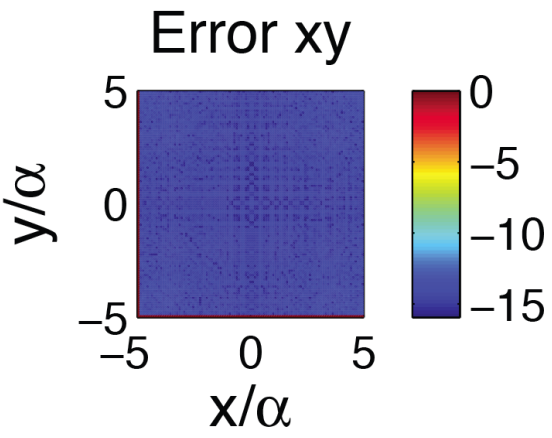

Figure 15: σ_{xy} error using Equation 27. Note that practically all points in the field are 0. The points that are not 0 resemble the small amount of error in our model. Visualization is plotted on a $\log_{10}$ scale to accentuate detail.

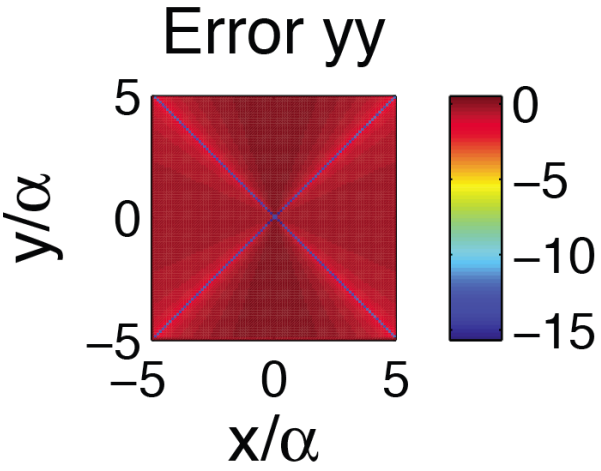

Figure 16: σ_{yy} error using Equation 27. Note that practically all points in the field are 0. The points that are not 0 resemble the small amount of error in our model. Visualization is plotted on a $\log_{10}$ scale to accentuate detail.

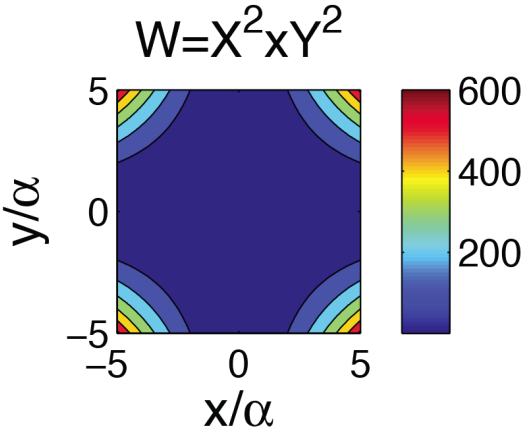

Figure 17: σ_{zz} error using Equation 27. Note that practically all points in the field are 0. The points that are not 0 resemble the small amount of error in our model. Visualization is plotted on a $\log_{10}$ scale to accentuate detail. Note that the corners are very large and are probability resultant from noise in the script. These regions have a large relative error.

3.3 Magma Propagation Criteria

McGovern et al. (2013) and Rubin (1995) define three criteria to evaluate the magma ascent through the lithosphere in vertical dikes. These criteria are based on the principles that dike intrusions perpendicular to the direction of least comprehensive principal stress, that enough tension is present in that direction for the rocks to crack, and that there is a vertical pressure gradient that forces magma upwards to the surface. The criteria are formally written as follows:

Equation 30: $$\Delta\sigma_{y_{top}} > \sigma_{local}$$

Equation 31: $$\Delta\sigma_{y_{bottom}} > \sigma_{local}$$

Equation 32:
$$\frac{d\Delta\sigma_y}{dz} = \frac{(\Delta\sigma_{y_{top}} - \Delta\sigma_{y_{bottom}})}{h} > 0$$

Where $\Delta\sigma_y$ is defined as the tectonic stress by Rubin (1995); it is the difference of vertical normal stress (σ_z) and horizontal normal stress perpendicular to the dike (σ_y), therefore $\Delta\sigma_y$ is defined as $\sigma_y - \sigma_z$. (30) and (31) express that enough tension should be present, at either the tip of the bottom of the plate, to exceed a local stress threshold value, σ_{local}, due to an assortment of factors such as regional stresses, and local inhomogeneities. However, based on the low tensile strength of highly damaged rocks in planetary lithospheres (Wieczorek et al., 2013) and on the absence of constraints on regional stress, I am taking σ_{local} to be zero, requiring both $\Delta\sigma_{y_{top}}$ and $\Delta\sigma_{y_{bottom}}$ to be positive in order for a dike to form.

In (32), the stress gradient must be positive for magma ascent to occur. At the top of the plate, differential compression must be at its smallest, and should increase with increasing depth. If compression is lowest at the bottom of the plate, magma ascent will be more restricted at larger depth as it ascends to the surface. The magma will experience an increasing horizontal compression as it ascends from its source, and it will eventually be pinched out before it reaches the surface of the plate. Therefore, magma must be 'positively buoyant' for it to be forced upward through the dike as opposed to downward (*Rubin, 1995)*.

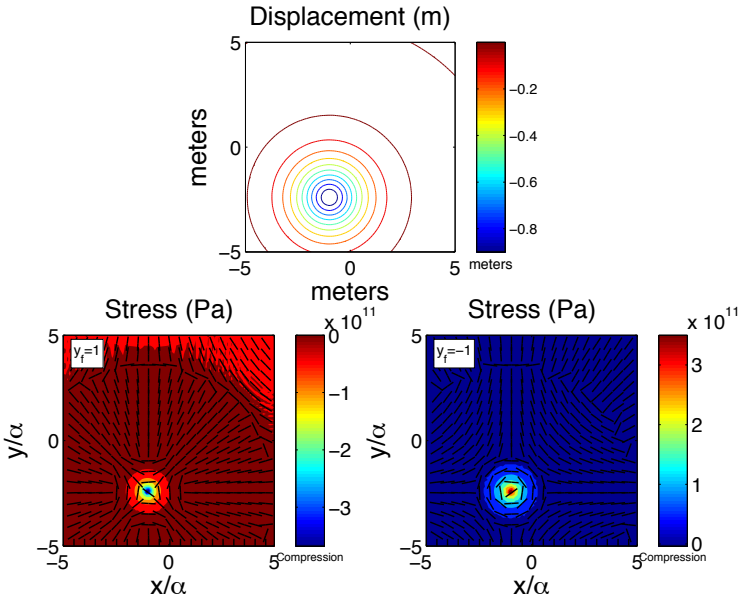

Figure 18:A top-down view of the displacement from a point source (top), and the compression and tension shown at the top and the bottom of the plate, respectively.

Gravitational acceleration	g	3.811	$\frac{m}{s^2}$
Mantle density	ρ_l	3500	$\frac{kg}{m^3}$
Basaltic Magma density	ρ_m	2700	$\frac{kg}{m^3}$
Crustal density	ρ_c	2900	$\frac{kg}{m^3}$
Young's Modulus	E	10^{11}	Pa
Poisson's Ratio	ν	0.25	

Table 1: Input values used in model

3.3.1 Verified Criteria

To affirm and test (30) and (31), the first two magma ascent criteria, the stress fields are evaluated for regions where the tectonic stress ($\Delta\sigma_y$) is positive. In accordance with our axisymmetric displacement function, we see an axisymmetric response in the stresses shown in *Figures 10-13*, and therefore an axisymmetric orientation of the tectonic stresses. In *Figures 19-20*, the respective magma ascent criteria are verified where the tectonic stresses are positive. These regions are expectedly located in an axisymmetric distribution about the area of loading.

To test (32), the third magma ascent criterion, the gradient of tectonic stress throughout the plate, and variations in magma pressure were evaluated in regions where there were positive. If differential stress decreases from the bottom to the top of the plate, dikes are able to form from the large amounts of tension experienced at the bottom of the plate. This tension forms cracks through work magma ascent can initiate. As the magma rises through the plate, it experiences a decrease in horizontal stresses, therefore encouraging upward motion towards the surface. *Figure 21* shows region where this scenario is positive and possible; again in an axisymmetric orientation about the area of loading.

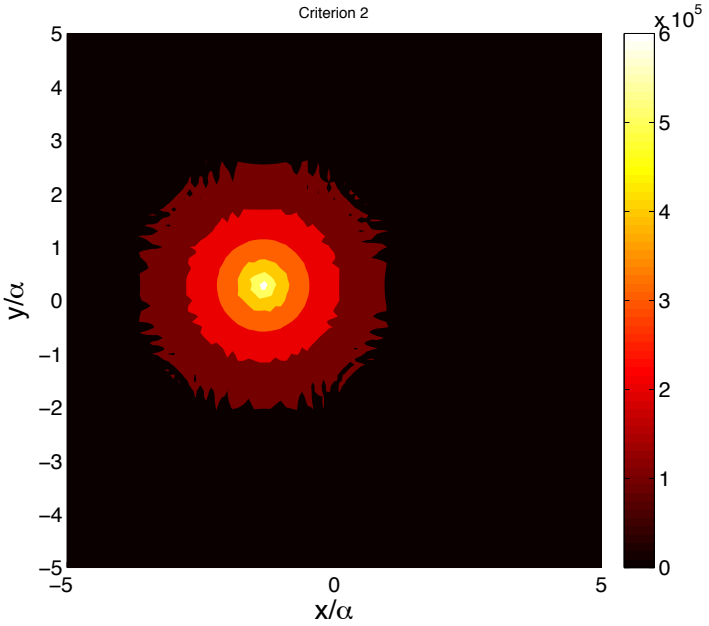

Figure 20: Regions where the second magma ascent criterion, expressed by (31), are verified at the bottom of the plate. The more positive a region is, the larger the tectonic stress is. Therefore, regions where the tectonic stress is large are where the criterion is more verified.

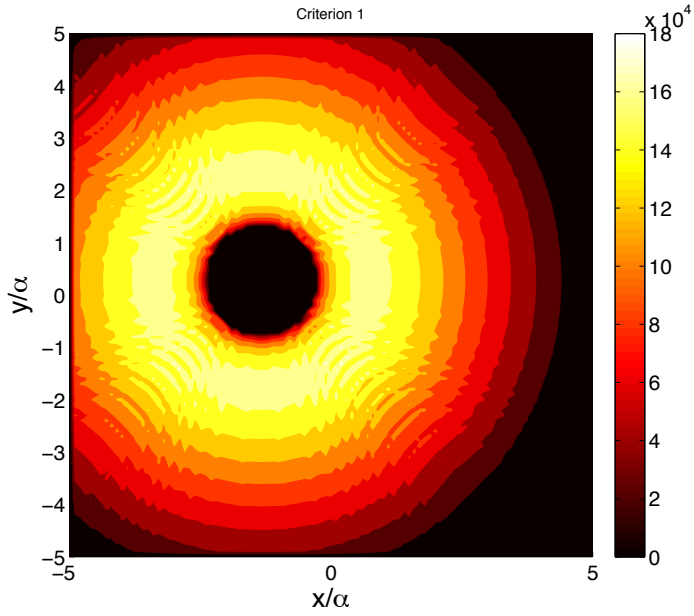

Figure 19: Regions where the first magma ascent criterion, expressed by (30), are verified at the top of the plate. The more positive a region is, the larger the tectonic stress is. Therefore, regions where the tectonic stress is large are where the criterion is more verified.

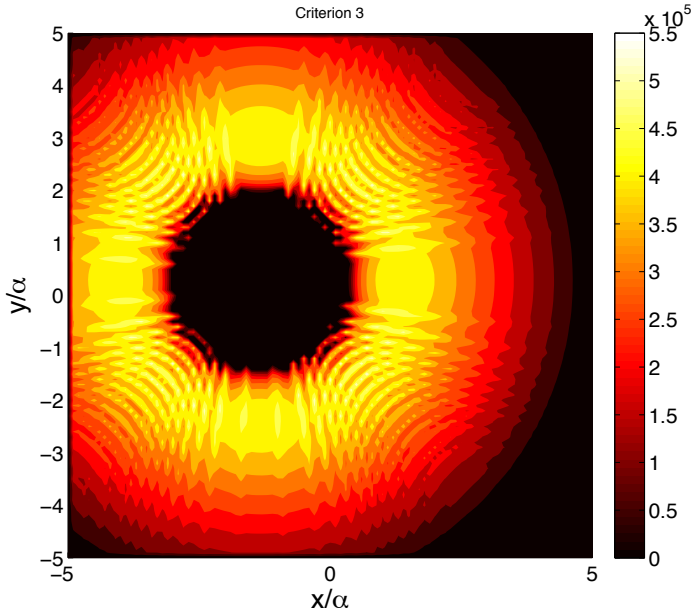

Figure 21: Regions where the third magma ascent criterion, expressed by (32), are verified throughout the plate. The more positive a region is, the larger the difference in tectonic stresses is. Therefore, regions where the differential compression increases towards the top of the plate are where the criterion is more verified.

3.3.2 Total Score

Magma ascent is likely to occur in regions where the most magma ascent criteria are verified. There are regions where three and two criteria overlap and are both verified, and there are regions where only one sole criterion is verified. These regions were assigned a score, from three to one, depending on how many criteria were verified in that location. The regions of scoring are axisymmetric in their locations, reflecting the axisymmetric nature of the stresses in the plate. The scoring of the deflected region is shown in *Figure 22.*

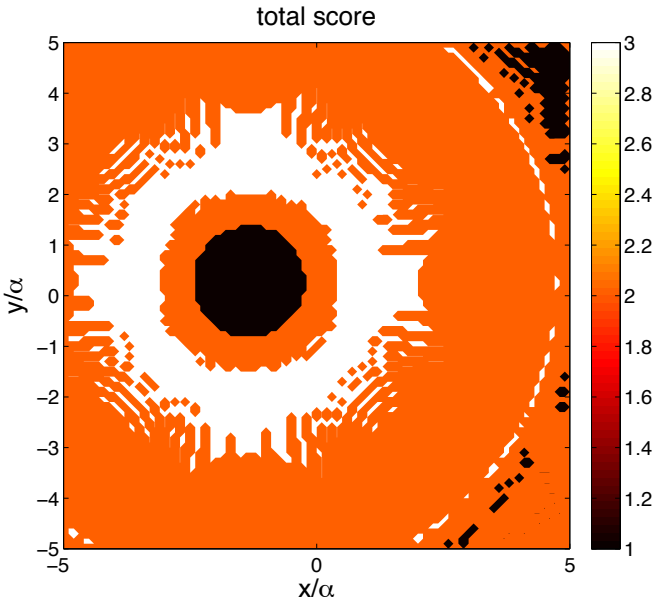

Figure 22: Regions where one criterion, or multiple criteria overlap and are verified are given a 'score' of one, two, or three. Magma ascent is likely to occur in regions where all three ascent criteria are verified, shown in white with a 'score' of three.

3.4 Site Sample Statistics

As noted in the visualizations in sections 3.3.1 and 3.3.2, the regions where all three magma ascent criteria are verified are oriented axisymmetrically about the area of loading. Therefore we must use statistical methods to choose the location where the next load is likely to be emplaced. The next load has equal potential to be emplaced in any region where all three criteria are verified. The location of the next load is determined by randomly sampling a statistical distribution of emplacement positions described by its probability distribution function (PDF). Two different distributions of potential eruptive sites are considered. Each new point is checked for its score. If the score is three, the coordinates of the point are recorded, a new load is emplaced at that position, the flexure calculation is updated, and another random point is selected. If the score of the point is not three, the location is removed from the pool, and the script moves onto the next randomly selected point.

3.4.1 Uniform Probability

In one of the probability density functions, a uniform density of sampling points was applied to the scored regions of criteria. This sampling distribution considers a uniform density of points throughout the radius of potential eruptive sites. Therefore, the probability of any point in this area to be an eruptive site can be expressed as:

Equation 33: P is constant

With the P being the probability, and r being the radial distance of a potential eruptive site to the source. This probability is verified if $r < r_0$, with r_0 being the radius of the entire magma source. The radius of our magma source is taken to be 3α. *Figure 23* shows this cumulative probability function applied within a circle with radius r_0, and a radial slice (θ) of the circle from 0 to r_0.

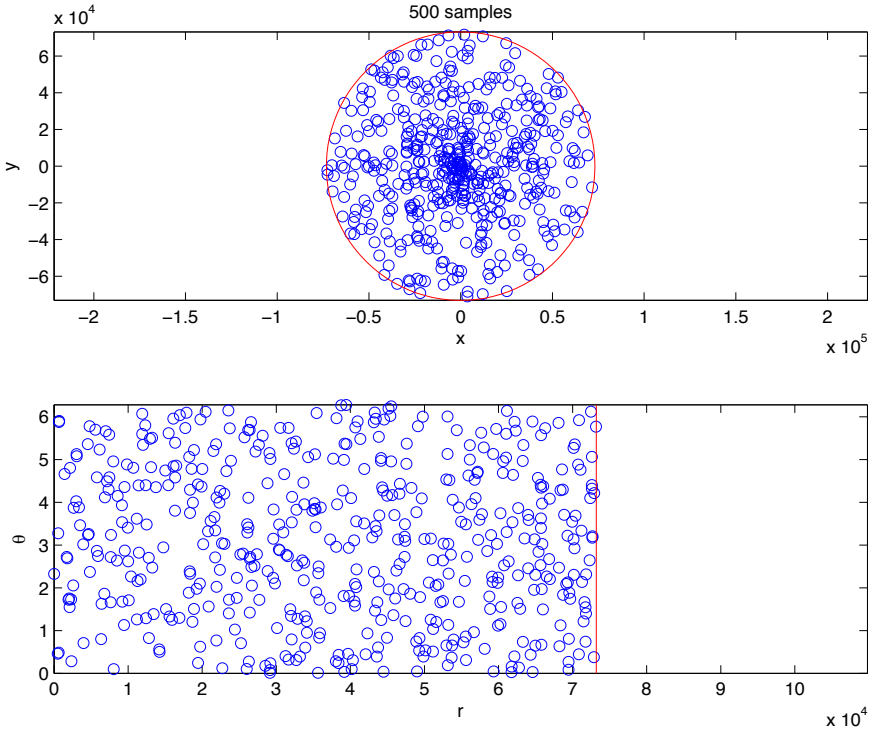

Figure 23: A visualization of 500 sampling points (ns=500) distributed with uniform density about a circle (top) with radius r_0, the radius of a potential magma source. Each one of these points will be randomly tested as potential eruptive sites if they have a score of three. It appears as through there is a uniform distribution of points throughout the circle, however, when a radial slice of the distribution is taken (bottom), the distribution shows a lower density of points near the center of the circle, and a higher density towards the outer edges of the magma source. This is because the points are distributed equal to the radial distance from the source, and not uniformly distributed with increasing radial distance.

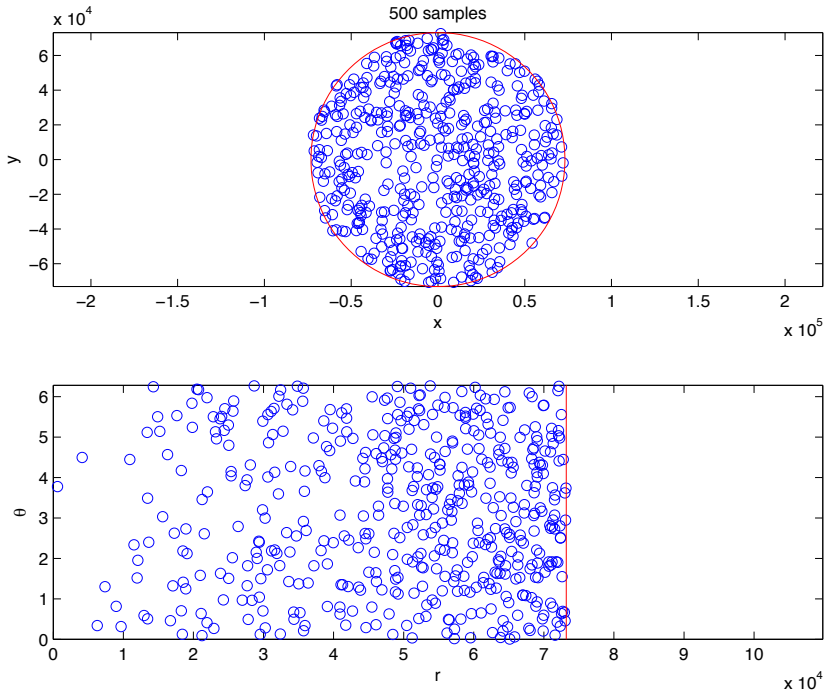

Figure 24: A visualization of 500 sampling points (ns=500) distributed with uniform density about a circle (top) with radius r_0, the radius of a potential magma source. Each one of these points will be randomly tested as potential eruptive sites if they have a score of three. It appears as through there is a higher concentration of points near the center of the circle, however, when a radial slice of the distribution is taken (bottom), the distribution is uniform. This is because the points are evenly distributed with radial distance from the source, and not uniformly distributed per unit area of the circle.

3.4.2 Probability Proportional to Area

For the other probability density function considered here, a probability proportional to unit area was applied to the scored regions of criteria. This sampling distribution considers a non-uniform density of points throughout the radius of potential eruptive sites. Therefore, the probability of any point in this area to be an eruptive site can be expressed as:

Equation 34: $P = r$

With the *P* being the probability, and *r* being the radial distance of a potential eruptive site to the source. Therefore, the larger the radius is from the source, the larger the density, and the higher the cumulative probability. This probability is also verified if $r < r_0$, with r_0 being the radius of the entire magma source. The radius of our magma source is taken to be 3α. *Figure 24* shows this cumulative probability function applied within a circle with radius r_0, and a radial slice (θ) of the circle from 0 to r_0.

4. Results

4.1 Load Updates

The case of a single point load is initially considered in the beginning our main loop. For this one point, its respective displacement is modeled (*Figure 9*), and its flexure-induced stress components (*Figures 10-13*), and principal stress directions are calculated (*Figure 18*). These stress components dictate how and where magma ascent and consecutive emplacement can occur (30)-(32). Applying the cumulative probability functions (33) and (34), we are able to determine where the next load will be emplaced. With each consecutive emplacement, the overall displacement will change, as well as all of the respective flexure-induced components. The stress-field, principal stress directions, and magma ascent criteria are re-calculated with each consecutive load. Furthermore, the magma score of each region changes with every new load, and the cumulative probability functions are re-applied to determine where the following load will appear.

4.1.1 Load Geometry

The displacement caused by a load at one given point, is shown in the above example of *Figure 9*. This approximation works well mathematically, but the loads in this experiment need to have geologic analogues. Brotchie and Silvester [1969] clearly set the playing field for steady state, analytic solutions of deflection from axisymmetric point loading, which can be found in Section 5.1.2. These solutions for concentrated loading were taken further by Wolf [1984], Watts et al., [1975] and Lambeck [1980], whom all considered loading from different geometries. In our examples of loading, we are considering the potential volcanic load increment to be a large cylinder, of dimensions W_l*=100 m* and R_l *=10 km*, with W_l and R_l being the height and radius of the cylinder, respectively. Examples of this cylindrical loading can be found in Watts [2001] *pp. 110-111*.

Deflection (w) of circular plates for a concentrated load *P* is defined as:

Equation 35: $w = \left(\frac{P\alpha^2}{2\pi D}\right) kei\left(\frac{r}{\alpha}\right)$

The load *P* is a force (which can be described as a weight) from each consecutive load applied to areas atop the plate. These forces can overlap in areas where consecutive magma piles are emplaced, eventually leading to the formation of topographic profiles. We define the force of concentrated load *P* as:

Equation 36: $P = \rho_l g\, dA$

g is the gravitational acceleration at the surface of Mars, ρ_l is the density of the lava that makes up each magma pile, and *dA* is the area on the grid over which the force is applied. In the simulations, I assume that the magma source (*r0*) is roughly 25-50 km in size, that the eruption radius (*rE*) is 10 km, and that each magma pile has a thickness (*Le*) of 50-100 m.

4.1.2 Step Growth (Uniform Probability)

Thirty consecutive loads are emplaced atop a plate of thickness T_e=*1 km* and the evolving deflection, lava pile thickness, and topography are visualized in *Figure 25*. Uniform density function (33) was used as a probability density function for site sampling.

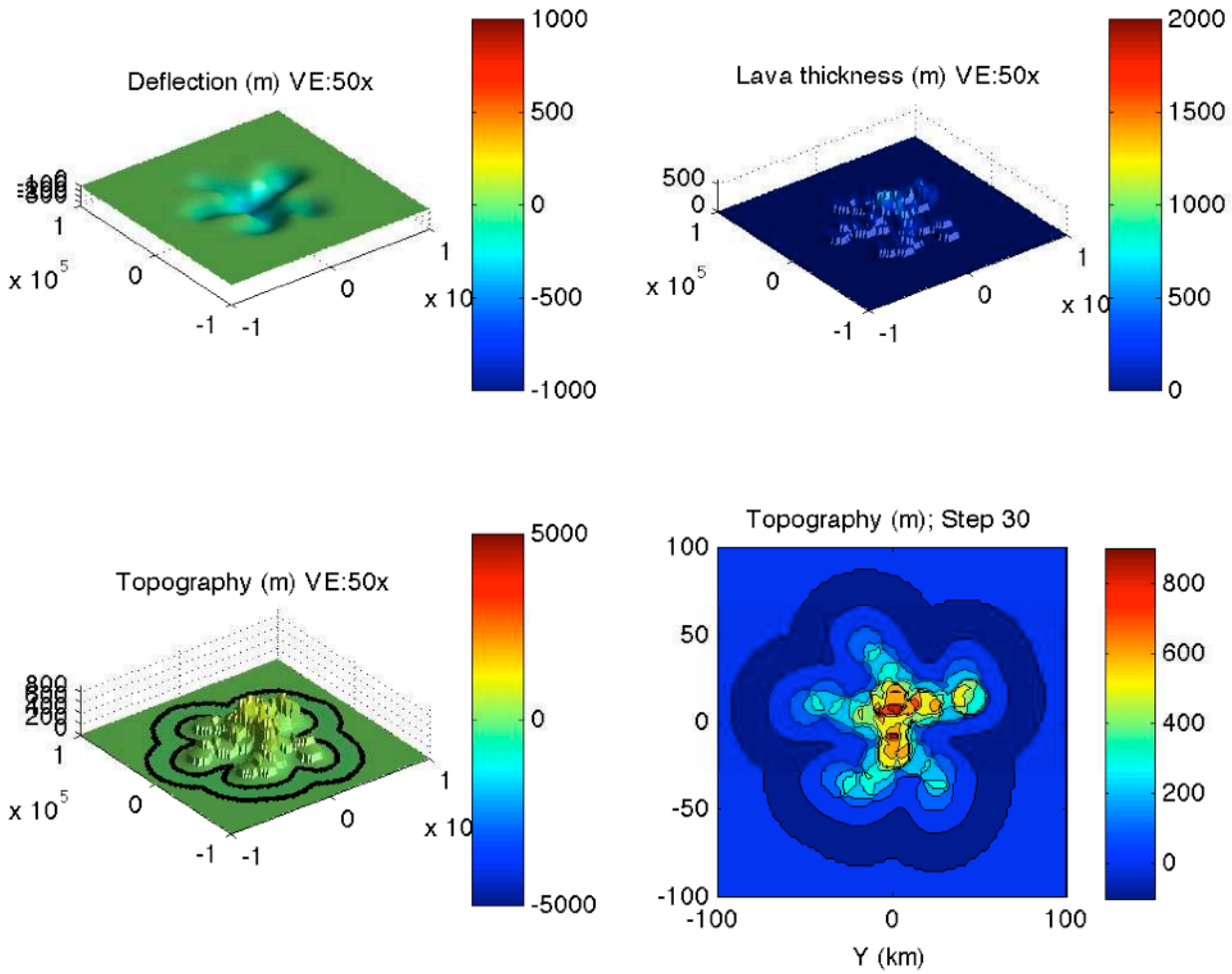

Figure 25: Consecutive deflection, lava pile thickness, topography, and topographic contours of a 30-step size edifice with 50x VE using a uniform probability site sampling method. Note the dendritic nature of where consecutive loads were emplaced.

4.1.3 Step Growth (Probability Proportional to Area)

Thirty consecutive loads are emplaced atop a plate of thickness T_e=*1 km* and the evolving deflection, lava pile thickness, and topography are visualized in *Figure 26*. Probability proportional to area equation (34) was used as a probability density function for site sampling.

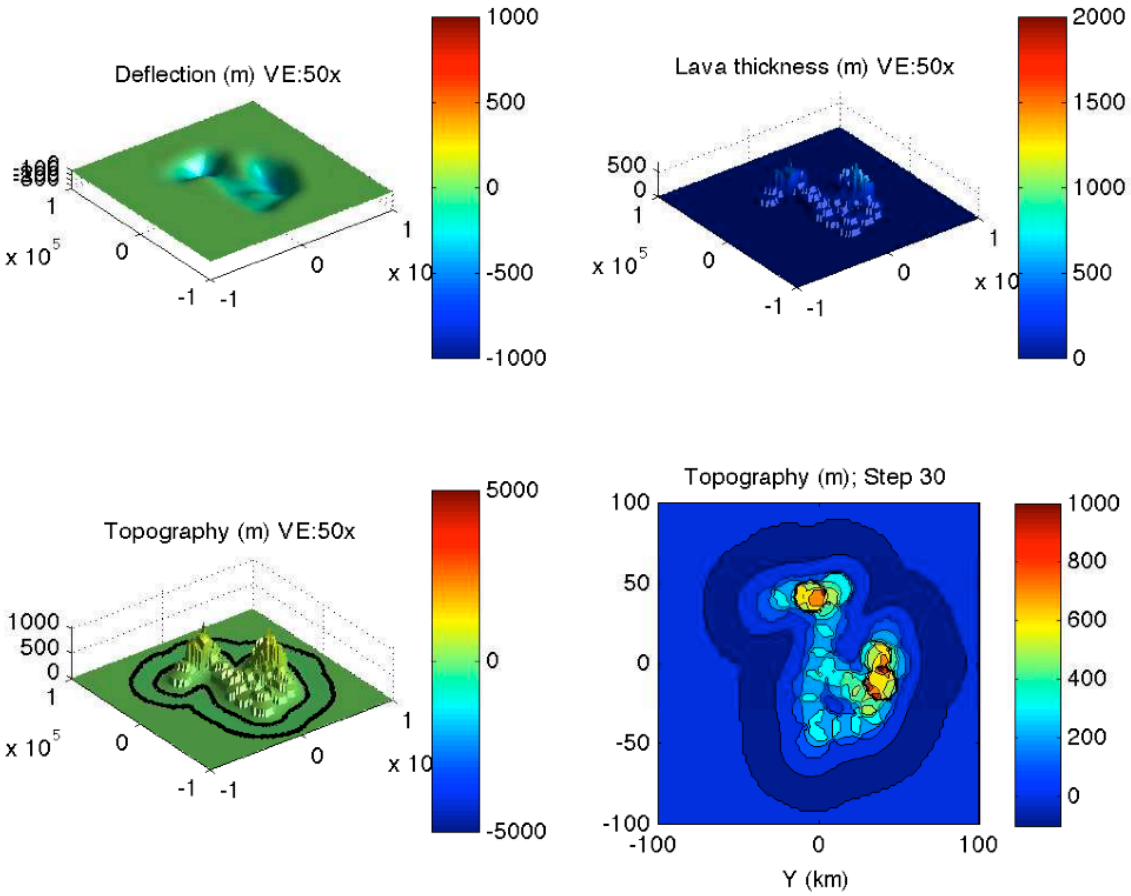

Figure 26: Consecutive deflection, lava pile thickness, topography, and topographic contours of a 30-step size edifice with 50x VE using a probability proportional to area site sampling method. Note the somewhat irregular and de-centralized nature of where consecutive loads were emplaced.

4.2 Variable Plate Thickness

I predict that that there is a correlation between the shape of a volcanic edifice, and the elastic thickness of the underlying lithosphere. For one of the final steps in my experiment, I setup my main loop to place an initial magma load atop a plate of a given thickness, and have the script calculate the deflection, the stress orientations, the magma ascent criteria, the score, and the statistically probable location of the next load for 200-400 consecutive loads in each loop. I ran this loop multiple times with varying values of *r0, rE, Le, T_e,* with each of the two probability density functions ((33) and (34)) applied, and visualized the result growth final topographic form that the consecutive magma piles (loads) formed.

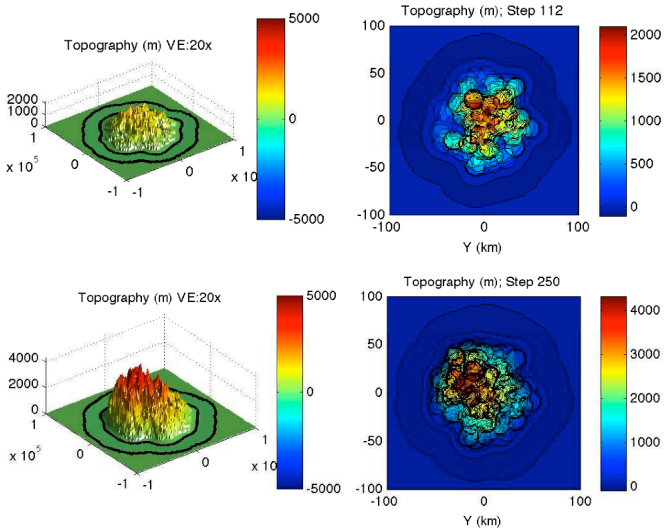

Figure 27: Topography of volcano at steps 112 and 250 atop a very thin plate of 500 m. Input variables: 50 km magma source radius, 10 km eruption radius, and site sampling is uniform. Note the mote defined by the black lines surrounding the edifice base.

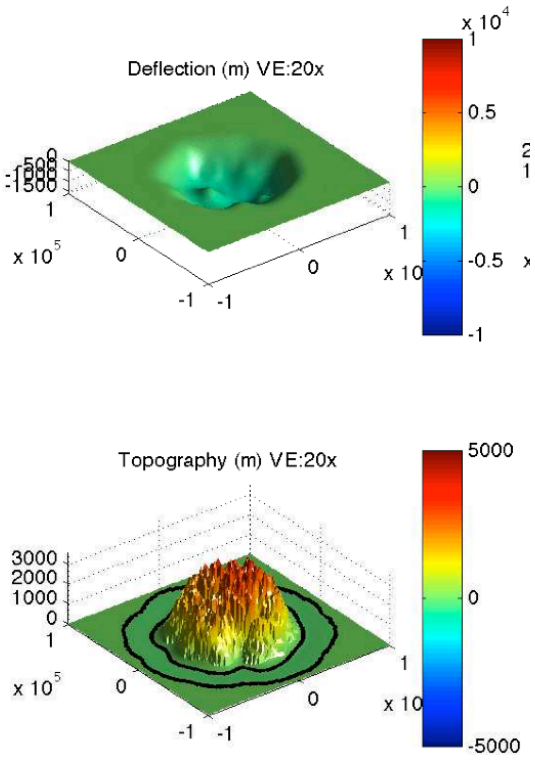

Figure 28: Plate deflection and topography of volcano at step 250 atop a plate of 1 km. Input variables: 50 km magma source radius, 10 km eruption radius, and site sampling is proportional to area

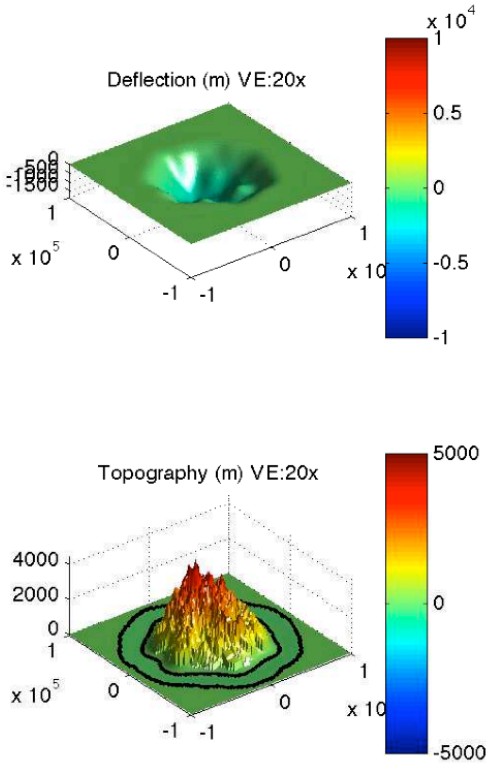

Figure 29: Plate deflection and topography of volcano at step 250 atop a plate of 1 km. Input variables: 50 km magma source radius, 10 km eruption radius, and site sampling is uniform throughout. Note that the choice of the site-sampling function made the topographic relief of the edifice slightly larger than the edifice in Figure 28. Also note that the radial extent of the edifice is slightly smaller than the edifice of Figure 28

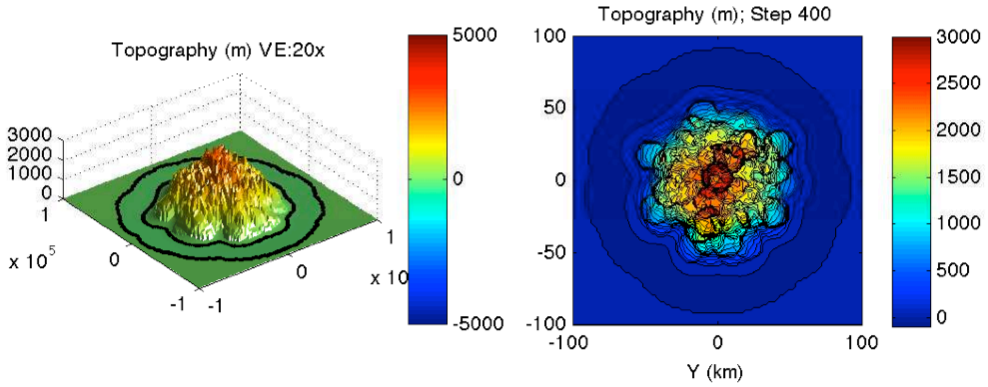

Figure 30: Topography and topographic contours of volcano at step 400 atop a plate of 10 km. Input variables: 50 km magma source radius, 10 km eruption radius, and site sampling is uniform. Note that the overall topographic relief is lower than Figures 31-32, and that the topographic contours are more diffuse at the edge of the edifice. A more prominent mote/annular trend is apparent in the region surrounding the base of this edifice.

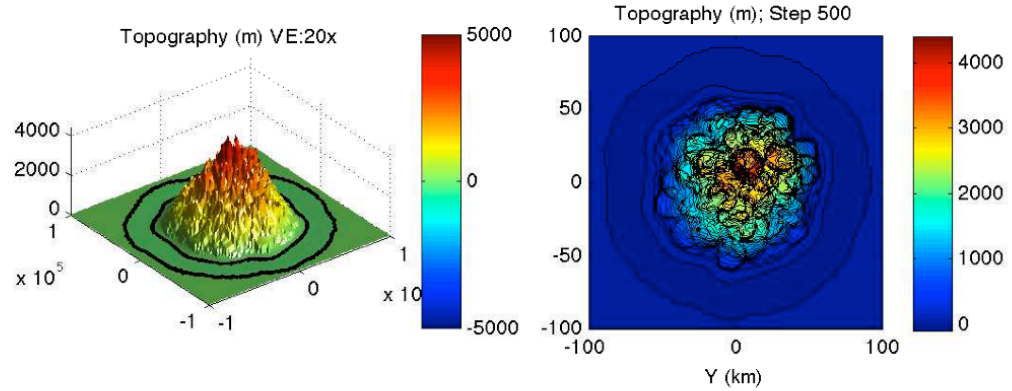

Figure 31: Topography and topographic contours of volcano at step 500 atop a plate of 40 km. Input variables: 50 km magma source radius, 10 km eruption radius, and site sampling is uniform. Note that with a thicker plate, the edifice becomes higher in elevation, and it forms more steeply flanking sides.

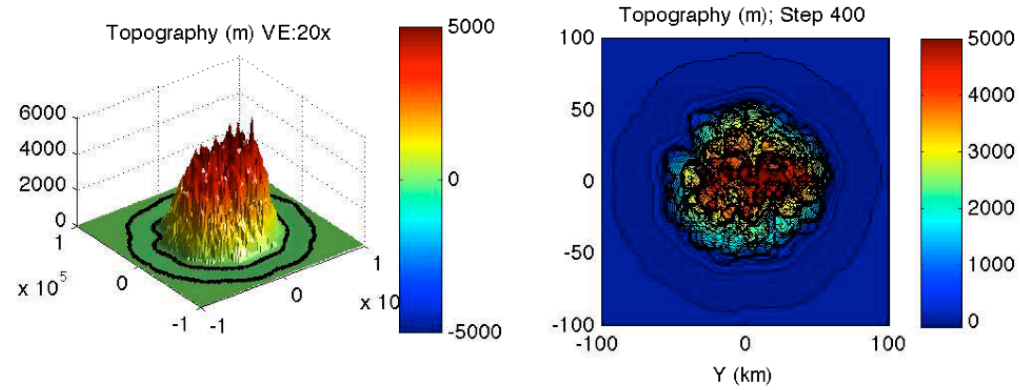

Figure 32: Topography and topographic contours of volcano at step 400 atop a plate of 60 km. Input variables: 50 km magma source radius, 10 km eruption radius, and site sampling is uniform. Note that with this thick plate, the edifice becomes even higher in elevation, and has very steep flanks. As the plate has thickened from the visualizations in Figures 30-32, the edifice profiles have become less flat, have grown in elevation, and have evolved to be more domical and conical in nature.

4.3 Applications to Martian Volcanoes

Elysium Mons is an example of a conical edifice on Mars. The steeply flanked sides, moderate topographic relief, and radial dike geometries are all similarities that can be seen in our model (*Figure 32*). This indicates emplacement at a high T_e, which is supported by T_e measurements in the region obtained by McGovern, et al., (2012).
The domical shapes of the Tharsis Montes are great examples of the truncated cone classification of the domical shape. We see emplacement of these at intermediate T_e values (*Figure 31*). The moderately sloped flanks, relatively flat top, and diffuse radial extent are all characteristics seen in both the model and on Mars.
The flat annular shapes of Patera-type volcanoes bear strong similarities with the Patera load model (*Figure 30*). Low topography, with a broad radial extent, and loose lobes /flows around the outer flanks of the edifice are all similarities seen in both the model, and to Patera volcanoes on Mars such as Thyrrhena Patera (*Figure 2*).

5. Summary

I have applied three types of stress-based magma ascent criteria to the flexure-induced stresses from axisymmetric loading atop a lithosphere modeled as a thin elastic shell. With the magma ascent criteria applied and scored, consecutive loads were chosen by the use of two probability density functions; uniform site-sampling with constant probability, and site-sampling with probability proportional to area. Each of these two sampling methods had an effect on the outcome of the edifice shape (*Figures 25-26*), however, not enough to change the overall edifice classification. There appears to be a range of T_e for each edifice shape; High values of T_e (i.e., $T_e > 40$ km), result in low stress gradients in the plate, allowing conical edifices to from flows originating anywhere on the edifice. For intermediate values of T_e (i.e., 15 km $< T_e <$ 40 km), high stress gradients throughout the plate, and comprehensive stresses in the lower lithosphere tend to cut off magma ascent near the center of a conical edifice, therefore creating a more domical edifice. At the lowest values of T_e (i.e., $T_e <$ 40 km), large stress gradients cut off practically all central magma ascent, inhibiting the growth of either a conical or domical edifice. However, the narrowly spaced zones in which the lithosphere experiences short-wavelength deflections lead to the formation of flat annular edifices. Therefore, my hypothesis is verified!

My work only considers a purely self-consistent loading scenario, with the deflection, stress gradients, and magma ascent criteria recalculate with each consecutive load. The loads used in this model were strictly surface-loads, and these methods do not include subsurface loading from viscous or other mechanisms. Despite my experiments application of only one loading mechanism/scenario, the verification of my model suggests that elastic deformation from flexure-induced stresses is a primary influence in volcanic edifice morphology.

Further implications can be drawn on global, regional, and local thermal gradients across and throughout the Martian surface and lithosphere. These thermal contractions can provide better insight into the rates of cooling of terrestrial bodies, and more specifically, the variable rate(s) of thickening of the Martian lithosphere.

6. Bibliography

Banerdt, Bruce W., Matthew P. Golombek, Kenneth L. Tanaka. "Stress and Tectonics on Mars". **Mars** (1992): *pp*. 249-297.

Brotchie, J. F., and Silvester, R., 1969. **On crustal flexure**. J. Geophys. Res., *vol*. 74, *pp*. 5240-5245.

Buz, J., McGovern, J.P., 2010. **Venusian volcano shapes: Implications for edifice evolution and the thermal state of Venus.** 41st Lunar and Planetary Science Conference, *1482*

Comer, P.R., 1983. **Thick plate flexure.** Geophys. J. R. astr. Soc., *vol. 72, pp. 101-113*

Comer, P.R., et al., 1985. **Mars: Thickness of the Lithosphere from the Tectonic Response to Volcanic Loads.** Review of Geophysics, *vol. 23, no. 1, pp. 61-92*

Lambeck, K., 1981. **Flexure of the ocean lithosphere from island uplift, bathymetry and geoid height observations: the Society Islands.** Geophys. J. R. astr. Soc., *vol. 67, pp. 91-114*

Hartmann, W. K., 1999. **Evidence for recent volcanism on Mars from crater counts**. Nature., *vol. 397, pp. 586-589*

Montési, L. G. J., Zuber, M. T., 2003. **Clues to the lithospheric structure of Mars from wrinkle ridge sets and localization instability**. J. Geophys. Res., *vol. 108, no. E6,* 5048

McGovern, J.P., et al., 2013. **The influence of lithospheric flexure on magma ascent at large volcanoes on Venus.** J. Geophys. Res. Planets, *vol. 118, pp. 2423–2437*

McGovern, J.P., et al., 2002. **Localized gravity/topography admittance and correlation spectra on Mars: Implications for regional and global evolution.** J. Geosphs. Res. *vol. 107, no. E12, 5136*

Rubin, M. A., 1995. **Propagation of magma-filled cracks.** Annual Review Earth and Planetary Sciences. *vol. 23, pp. 287-336*

Turcotte, Donald L., and Gerald Schubert. **Geodynamics**. Cambridge, MA: Cambridge University Press, 2002.

Watts, A. B., **Isostasy and Flexure of the Lithosphere**. Cambridge, MA: Cambridge University Press, 2001

Watts, A. B., et al., 1975. **Gravity Anomalies and Flexure of the Lithosphere: A Three-Dimensional Study of the Great Meteor Seamount, Northeast Atlantic.** J. Geophys. Res., *vol. 80, no.11, pp. 1391-4116*

Weller, C., 2012. **Origin of the variation of amplitude of the Hawaiian swell.** UMD GEOL393, Spring 2014.

Werner, C. S., 2009. **The global Martian volcanic evolutionary history.** Icarus. *vol. 201, pp. 44-68*

Wolf. D., 1984. **On the relation between two-dimensional and axisymmetric loads in plate flexure problems.** J. Geophys. Res., *vol. 54, pp. 232-235*

7. Appendices

Appendix A

MATLAB function used to define KEI

```
function [out]=KEI(x)
X=[0:0.1:10];
K=[-0.785398163
-0.776850647
-0.758124933
-0.733101912
-0.703800212
-0.671581695
-0.637449495
-0.602175452
-0.566367651
-0.530511122
-0.494994637
-0.460129528
-0.426163604
-0.393291827
-0.361664782
-0.331395562
-0.302565474
-0.275228834
-0.249417069
-0.225142235
-0.202400068
-0.181172644
-0.161430701
-0.143135677
-0.126241488
-0.110696099
-0.096442891
-0.083421858
-0.071570649
-0.060825473
-0.051121884
-0.042395447
-0.034582313
-0.027619697
-0.021446287
-0.016002569
-0.011231096
-0.007076704
-0.003486665
-4.11E-04
0.002198399
0.004385818
0.006193613
0.007661269
0.008825624
0.009720919
0.010378865
```

```
0.010828725
0.011097399
0.011209526
0.011187587
0.011052008
0.010821278
0.010512056
0.010139286
0.009716307
0.009254964
0.008765716
0.008257737
0.007739025
0.007216492
0.006696059
0.006182749
0.005680767
0.005193579
0.004723992
0.004274219
0.003845946
0.003440398
0.003058385
0.002700365
0.002366486
0.002056629
0.001770454
0.001507429
0.001266868
0.001047959
8.50E-04
6.71E-04
5.12E-04
3.70E-04
2.44E-04
1.34E-04
3.81E-05
-4.45E-05
-1.15E-04
-1.74E-04
-2.23E-04
-2.63E-04
-2.95E-04
-3.19E-04
-3.37E-04
-3.49E-04
-3.55E-04
-3.57E-04
-3.56E-04
-3.51E-04
-3.43E-04
-3.33E-04
-3.21E-04
-3.08E-04];
out=interp1(X,K,x);
end
```

Appendix B

MATLAB function to define σ_{yz}, σ_{xz}, and σ_{xy} stress components.

```
function [sigma_xx,errxx,sigma_yy,erryy,sigma_xy,errxy,sigma_zz,errzz,
sigma_xz,sigma_yz] = stress(W,Xm,Ym)
h=max(abs(Xm(1)-Xm(2)),abs(Ym(1)-Ym(2)));
E=1; % Youngs modulus
yf=1;   % distance from neutral surface to fiber
v=.25; % Poissons ratio

pxx = [1 -2 1]; %d^2w/dx^2
pxx=pxx/h^2;

pyy= [1 -2 1]'; %d^2w/dy^2
pyy=pyy/h^2;

pxy= [-1 0 1; %d^2w/dxdy
   0 0 0;
   1 0 -1];
pxy = pxy/(4*h^2);
pxy=flipud(pxy);

px=[-1 0 1]; %dw/dx
px = px/(2*h);

py=[-1 0 1]'; %dw/dy
py=py/(2*h);

wxx=zeros(size(Xm));
wyy=zeros(size(Xm));
wxy=zeros(size(Xm));
wx=zeros(size(Xm));
wy=zeros(size(Xm));


for i= 1:numel(Xm(1,:))
   for j=2:numel(Xm(1,:))-1
      wxx(i,j)=sum(sum(pxx.*W(i,j-1:j+1)));
      wyy(j,i)=sum(sum(pyy.*W(j-1:j+1,i)));
      wx(i,j)=sum(sum(px.*W(i,j-1:j+1)));
      wy(j,i)=sum(sum(py.*W(j-1:j+1,i)));
     if (i>1) && (i<numel(Xm(1,:)));
        wxy(i,j)=sum(sum(pxy.*W(i-1:i+1, j-1:j+1)));
     end
   end
end


lam=((E*v)/((1+v)*(1-2*v)));
mu=(E/(2*(1-v)));
```

```
sigma_xx=yf*((lam+2*mu)*wxx + lam*wyy);
sigma_yy=yf*(lam*wxx +(lam+2*mu)*wyy);
sigma_zz= yf*lam*(wxx+wyy);
sigma_xy=2*mu*yf*wxy;
sigma_xz=2*mu*wx;
sigma_yz=2*mu*wy;

%Visualizations


figure(3)
contour(Xm, Ym, sigma_xy)
title('sigmaxy shear stress','fontsize', 18)
xlabel('x/\alpha', 'fontsize', 18)
ylabel('y/\alpha', 'fontsize', 18)
zlabel('stress','fontsize', 18);
set(gca, 'fontsize',14);
axis equal;
contourcbar
print -dpdf sigmaxy_stress.pdf

figure(4)
contour(Xm, Ym, sigma_zz)
title('sigmazz stress','fontsize', 18)
xlabel('x/\alpha','fontsize', 18)
ylabel('y/\alpha','fontsize', 18)
zlabel('stress','fontsize', 18);
set(gca, 'fontsize',14);
axis equal;
contourcbar
print -dpdf sigmazz_stress.pdf

figure(5)
contour(Xm, Ym, sigma_xx)
title('sigmaxx stress','fontsize', 18)
xlabel('x/\alpha','fontsize', 18)
ylabel('y/\alpha','fontsize', 18)
zlabel('stress','fontsize', 18);
set(gca, 'fontsize',14);
axis equal;
contourcbar
print -dpdf sigmaxx_stress.pdf

figure(6)
contour(Xm, Ym, sigma_yy)
title('sigmayy stress','fontsize', 18)
xlabel('x/\alpha','fontsize', 18)
ylabel('y/\alpha','fontsize', 18)
zlabel('stress','fontsize', 18);
set(gca, 'fontsize',14);
axis equal;
contourcbar
print -dpdf sigmayy_stress.pdf
```

```
Wt=sqrt(Xm.^2+Ym.^2);
dxx=(Xm.^2)./(Wt.^3);
dyy=(Ym.^2)./(Wt.^3);
dxy=(Xm.*Ym)./(Wt.^3);

sigma_xxt=yf*((lam+2*mu)*dxx + lam*dyy);
sigma_yyt=yf*(lam*dxx +(lam+2*mu)*dyy);
sigma_zzt= yf*lam*(dxx+dyy);
sigma_xyt=2*mu*yf*dxy;
errxx=(abs(sigma_xxt-sigma_xx)./sigma_xx);
erryy=(abs(sigma_yyt-sigma_yy)./sigma_yy);
errzz=(abs(sigma_zzt-sigma_zz)./sigma_zz);
errxy=(abs(sigma_xyt-sigma_xy)./sigma_xy);

figure(9)
pcolor(Xm, Ym, errxx);
contourcbar
shading flat
title('sigmaxx stress','fontsize', 18)
xlabel('x/\alpha','fontsize', 18)
ylabel('y/\alpha','fontsize', 18)
set(gca, 'fontsize',14);
axis equal
print -dpdf errsigmaxx_stress.pdf

figure(10)
pcolor(Xm, Ym, erryy);
contourcbar
shading flat
title('sigmayy stress','fontsize', 18)
xlabel('x/\alpha','fontsize', 18)
ylabel('y/\alpha','fontsize', 18)
set(gca, 'fontsize',14);
axis equal
print -dpdf errsigmayy_stress.pdf

figure(11)
pcolor(Xm, Ym, errzz);
contourcbar
shading flat
title('sigmazz stress','fontsize', 18)
xlabel('x/\alpha','fontsize', 18)
ylabel('y/\alpha','fontsize', 18)
set(gca, 'fontsize',14);
axis equal
print -dpdf errsigmazz_stress.pdf

figure(12)
pcolor(Xm, Ym, errxy);
contourcbar
shading flat
title('sigmaxy stress','fontsize', 18)
xlabel('x/\alpha','fontsize', 18)
ylabel('y/\alpha','fontsize', 18)
set(gca, 'fontsize',14);
```

```
axis equal
print -dpdf errsigmaxy_stress.pdf

end
```

8. Acknowledgements

I would like to thank the UMD department of Geology for their comments, review, and time spent reading my work. I deeply appreciate the jokes that Dr. John Merck has told me. Dr. Doug Hamilton of the UMD Astronomy department has deeply provoked in me an interest in planetary sciences. Mark Larson has supported and criticized my work, expanding and furthering my knowledge and approach. Emily Rapp provides a basis of support unlike any other. Danny Serven is a logician and engineer from anther world. And of course, Dr. Laurent Montesi has shown constant support, in these endeavors, none of this work would have come to be without him.